A crack-tracking technique for localized cohesive-frictional damage

Savvas Saloustros [a *], Luca Pelà [a], Miguel Cervera [a]

[a] *International Center for Numerical Methods in Engineering (CIMNE),Universitat Politècnica de Catalunya (UPC-BarcelonaTech), Jordi Girona 1-3, 08034 Barcelona, Spain.*

Abstract – This paper extends the use of crack-tracking techniques within the smeared crack approach for the numerical simulation of cohesive-frictional damage on quasi-brittle materials. The mechanical behaviour is described by an isotropic damage model with a Mohr-Coulomb failure surface. The correct crack propagation among the two alternative fracture planes proposed by the Mohr-Coulomb theory is selected with the use of an energy criterion based on the total elastic strain energy. The simulation of three benchmark problems of mixed-mode fracture in concrete demonstrates that the proposed methodology can reproduce the material's frictional characteristics, showing robustness, as well as mesh-size and mesh-bias independence.

Keywords: Continuum Damage Model, Crack-Propagation, Cracking, Strain Localization, Mohr-Coulomb

---

* Corresponding author.

E-mail addresses: savvas.saloustros@upc.edu (Savvas Saloustros), luca.pela@upc.edu (Luca Pelà), miguel.cervera@upc.edu (Miguel Cervera).

Highlights:

- A new crack propagation criterion consistent with the Mohr-Coulomb theory.
- A local crack-tracking technique accounting for material's frictional behaviour.
- Crack propagation direction evaluated by an energy criterion.
- Numerical simulation of mixed mode tests on concrete specimens.

Nomenclature

Symbols	
c	cohesion
$\boldsymbol{C}$	isotropic linear–elastic constitutive tensor
d	damage index
D	specific dissipated energy
E	Young's modulus
f_t	tensile strength
f_c	compressive strength
G_f	tensile fracture energy
h_e	average element size
H_d	discrete softening parameter
H_{mat}	material softening parameter
l_{dis}	discrete characteristic width
l_{mat}	material characteristic length
l_e	finite element size
r	damage threshold internal variable
r_{excl}	exclusion radius defined by the user
r_{neigh}	radius of the neighbourhood where $\vec{V}_c$ is computed
r_{crack}	radius for the application of the energetic criterion.
r_{crit}	radius defined by the user used for the selection of r_{crack}

r_0	initial value of the damage threshold internal variable
v	Poisson's ratio
V^e	the volume of element e
$\vec{V}_e$	crack direction for the current element
$\vec{V}_c$	crack average direction vector
$\vec{V}_{c,max}$	vector which forms an angle a_{max} with vector $\vec{V}_c$
V_1, V_2	the volume of the potential cracks in the directions θ_1 and θ_2
w_1, w_2	the elastic strain energy per volume crack for crack propagation θ_1 and θ_2.
W^e	the elastic strain energy of element e
a	angle between $\vec{V}_c$ and $\vec{V}_e$
a_{max}	maximum curvature angle
β	angle between a potential failure surface and the direction of the minimum principal stresses
δ_κ	distance between *new potential* and *crack tip/root* element
$\theta_{1,2}$	direction of the two potential fracture planes according to the Mohr-Coulomb theory
Σ	equivalent stress
σ	normal stress
$\boldsymbol{\sigma}$	stress tensor

$\bar{\boldsymbol{\sigma}}$	effective stress tensor
τ	shear stress
$\boldsymbol{\varepsilon}$	strain tensor
ψ^e	the selected crack propagation angle of element *e*.
φ	internal friction angle
Φ	damage criterion
ω^e	direction of the minimum principal stresses of element *e*
:	double contraction

Abbreviations

DEN	Double Edge Notched
XFEM	Extended Finite Element Method
EFEM	Embedded Finite Element Method

1. Introduction

The accurate structural assessment of existing structures and the efficient design of new ones necessitate, apart from the comprehensive knowledge of the construction materials' characteristics, the realistic simulation of fracture phenomena, potentially leading to structural failure. Geomaterials, such as concrete, mortar and bricks, are typically found in the existing buildings. Owing to their high competence under compressive loading, the critical state in such materials is usually determined by their shear or tensile capacity. Under these two stress states, fracture initiates upon reaching the material's ultimate capacity and propagates exhibiting a drop in the stress (i.e. stress softening) for increasing strain. It is for this reason that these materials are termed as *quasi-brittle materials*.

Simulation of fracture in quasi-brittle materials within the computational failure mechanics is possible by means of two alternative ways: the discrete and the smeared crack approaches. In the discrete crack approach, cracking is modelled as an actual discontinuity within the finite element domain. On the contrary, in the discrete crack approach the onset and the propagation of the modelled crack bases on energy criteria. On the contrary, in the smeared crack approach the fracture is initiated by a stress/strain criterion and is modelled as smeared within the area of a finite element by modifying its mechanical properties (stiffness and strength). For a comprehensive review of discrete and smeared crack approaches the reader is referred to [De Borst 2001, Jírasek & Belytschko 2002, Karihaloo & Xiao 2003, Cervera & Chiumenti 2006a, Cervera & Chiumenti 2006b, Rabczuk 2012].

Independently of the approach chosen to simulate fracture, it was soon realised that the numerical solution was strongly dependent on the discretization characteristics of the analysed domain, i.e. there was a strong mesh-bias dependence. To overcome this drawback, the aforementioned numerical strategies are usually enhanced by means of an integrated crack-tracking procedure. The use of crack-tracking techniques permits to identify the path for the crack propagation and allow in this way the application of the selected numerical strategy on a restricted part of the mesh. This necessity for the prediction of the crack propagation has triggered the research on the methodology to identify the correct crack path. Within the discrete crack method, a variety of procedures have been proposed. These include on one hand the use of local criteria, where the crack propagates towards the direction of the maximum circumferential stress at the vicinity of the crack tip [Cendón et al. 2000, Stolarska et al. 2001, Moës & Belytschko 2002, Zi & Belytschko 2003] or perpendicular to the direction of the maximum principal stress of an averaged stress/strain tensor at the vicinity of the advancing crack [Wells & Sluys 2001, Jirásek & Zimmerman 2001]. On the other hand, global criteria have been proposed by Oliver and co-workers [Oliver & Huespe 2004, Oliver et al. 2004] and Meschke & Dumstorff [Meschke & Dumstorff 2007]. In the first methodology the crack-direction is determined by iso-lines running perpendicular to the maximum principal stresses, while in the latter both the crack orientation and extension are included as additional unknowns in the variational formulation. A comparison of the above methodologies is available in [Dumstorff & Meschke 2007]. The inventory of crack propagation criteria within the smeared crack approach is still narrow. In the first application of crack-tracking techniques within the

smeared approach Cervera & Chiumenti [Cervera & Chiumenti 2006a, Cervera & Chiumenti 2006b] determined the crack direction using the aforementioned global criterion of Oliver and co-workers [Oliver & Huespe 2004, Oliver et al. 2004]. Later, the concept of tracking of the crack path was applied at a local level [Cervera et al. 2010a] with the crack orientation determined to be perpendicular to the direction of the maximum principal stresses at the crack tip. Within this local criterion, spurious changes of propagation direction can be avoided by the opportune correction of the crack orientation based on potentially and consolidated damaged elements [Cervera et al. 2010a] or by means of delayed crack path fixation [Slobbe et al. 2014]. Another competent way for modelling strain localization within the smeared crack approach is the use of mixed stress/displacement or strain/displacement formulations [Cervera et al. 2010b, Cervera et al. 2010c Cervera et al. 2015, Benedetti et al. 2015]. An important feature of these mixed formulations is their general applicability to two and three-dimensional problems without the necessity of an auxiliary crack-tracking technique.

A common ground of the majority of the presented crack propagation criteria is the explicit or implicit assumption that the crack propagates in a direction perpendicular to the maximum principal stress direction. This hypothesis is consistent with the Rankine failure criterion, in which cracking occurs when the maximum stress reaches the tensile strength of the material on a plane orthogonal to the first stress eigenvector (see Figure 1). However, for a failure criterion different from Rankine's (e.g. Tresca or Mohr-Coulomb, see Figure 1), the failure condition is satisfied in two potential planes diverging from the direction of the minimum principal stresses by an angle β (Cervera et al. 2012, Wu &

Cervera 2015). Inevitably, these cases require a crack propagation criterion that a) is consistent with the used failure criterion and b) is capable to select the correct propagation direction between the two potential ones.

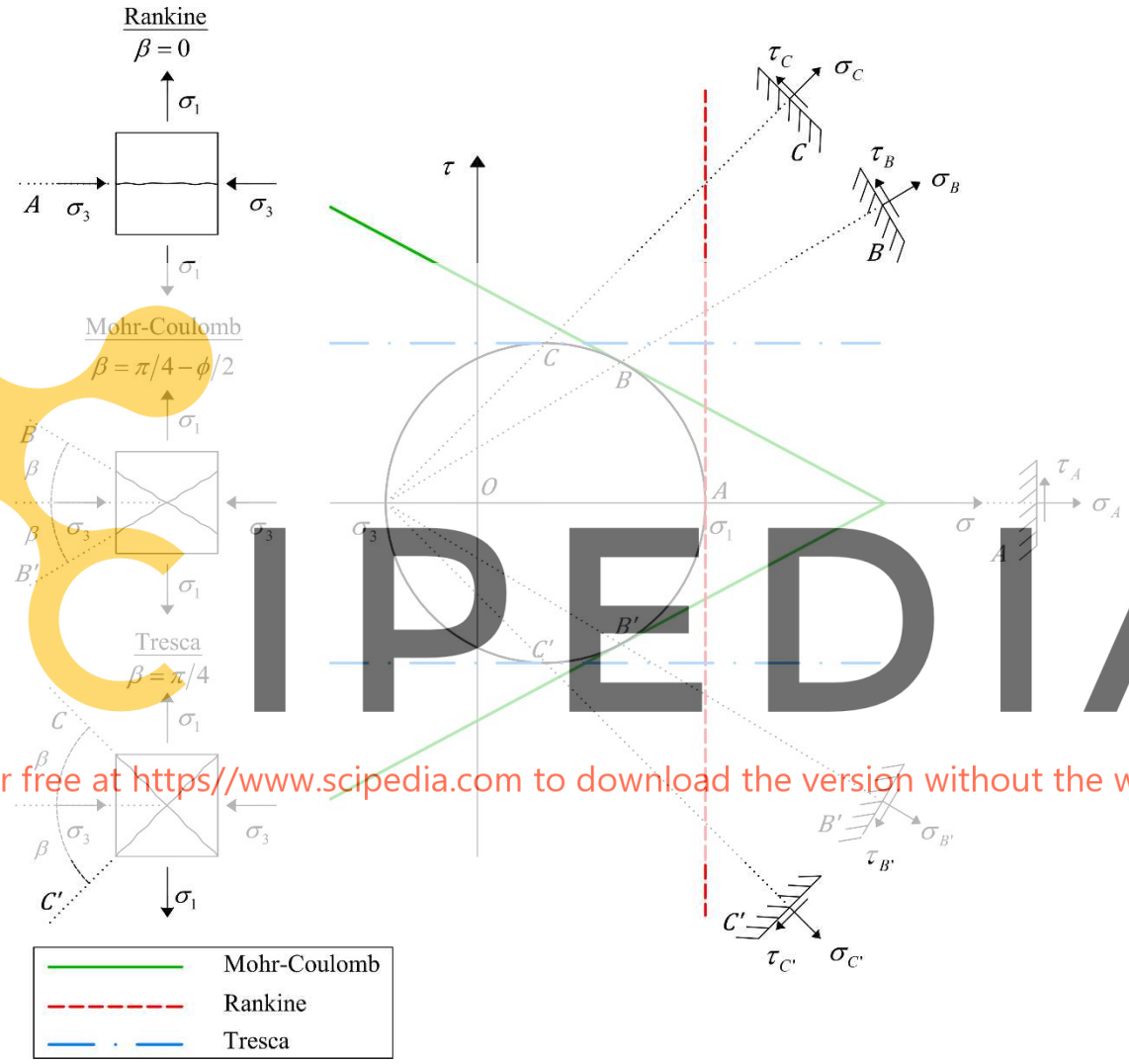

Figure 1. Failure planes of Mohr-Coulomb, Rankine and Tresca failure criteria in the σ, τ plane.

The aim of this work is to propose a crack-propagation criterion that is consistently connected to the assumed failure criterion. The study focuses on the simulation of fracture in

geomaterials, which present cohesive-frictional characteristics under shear failure. Therefore, cracks due to shear or tension are considered separately, with different propagation criteria for each case. Crack propagation in the direction perpendicular to the maximum principal stresses is attained only for the case of pure tension. Under shear, the crack propagation direction is defined according to the Mohr-Coulomb planes of failure. To this end, the answer to the dilemma on the correct selection among the two alternative potential fracture planes defined by the Mohr-Coulomb theory is sought with the use of an energy criterion based on the total elastic strain energy.

The paper is organized in the following way. Section 2 includes a brief review of the Mohr-Coulomb theory, as well as the description of the tensile and shear failures considered in this work. Section 3 presents an overview of the used continuum damage model. Then, the proposed local crack-tracking algorithm is described in detail in Section 4. Section 5 presents numerical examples for the validation of the algorithm's capacity to simulate the frictional characteristics in quasi-brittle materials. The paper ends with some concluding remarks in Section 6.

2. Criterion for crack initiation and propagation

2.1 The Mohr-Coulomb theory of rupture

Geomaterials such as rocks, concrete and mortar, exhibit quite different strength in tension and compression. As a consequence, the simulation of fracture in these materials requires a pressure dependent criterion. Such criterion occurs in the Mohr-Coulomb theory of failure. Mohr's postulate, dating from 1900, states that failure occurs on a plane where the normal (σ) and the shear (τ) stresses reach a critical combination. For isotropic

materials, in which the strength properties are the same when the shear stress is reversed, this critical combination can be expressed as:

$$f = \tau \mp g(\sigma) = 0 \tag{1}$$

A special case of Mohr's postulate is when the bounding curves $g(\sigma)$ are straight lines in the form of Coulomb's equation, dating from 1773:

$$g(\sigma) = c - \sigma \tan \varphi \tag{2}$$

where c is the cohesion and φ the internal friction angle of the material. The use of Coulomb's model of friction in Equation (1) results in the Mohr-Coulomb failure criterion:

$$|\tau| = c - \sigma \tan \varphi \tag{3}$$

In the σ, τ plane, Equation (3) represents two straight lines symmetrical to the σ-axis (see Figure 2). An alternative way for presenting Mohr-Coulomb's failure criterion is in terms of the principal stresses:

$$f(\sigma_1, \sigma_3) = \frac{\sigma_1}{f_t} - \frac{\sigma_3}{f_c} - 1 = 0, \qquad \sigma_1 \geq \sigma_2 \geq \sigma_3 \tag{4}$$

where f_t and f_c are the tensile and compressive strength of the material equal to:

$$f_t = \frac{2c \cos \varphi}{1 + \sin \varphi} \qquad\qquad f_c = \frac{2c \cos \varphi}{1 - \sin \varphi} \tag{5a-b}$$

From Equations (5a-b) the friction angle and cohesion can be expressed in terms of the tensile and the compressive strength:

$$\varphi = sin^{-1}\left(\frac{f_c/f_t - 1}{f_c/f_t + 1}\right), \quad 0 \leq \varphi < \frac{\pi}{2} \qquad\qquad c = \frac{1}{2}\sqrt{f_c f_t} \tag{6a-b}$$

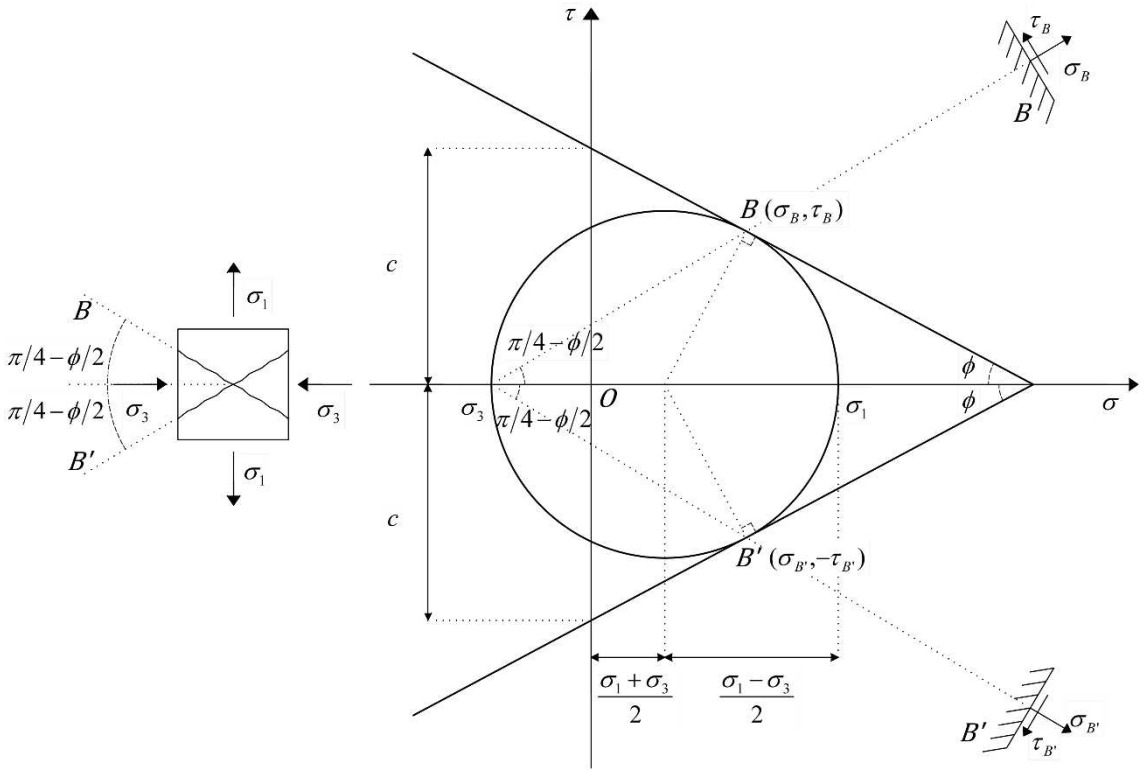

Figure 2. Mohr-Coulomb failure criterion in the σ, τ plane.

Figure 3 illustrates the dependence of the failure surface on the compressive to tensile strength ratio (or the friction angle and cohesion). As expected, for $f_c/f_t = 1$ ($\varphi = 0$) the Mohr-Coulomb failure criterion coincides with Tresca's hexagon. On the other end, a large compressive to tensile strengths ratio ($f_c/f_t \to \infty$ or $\varphi = \pi/2$) results in the coincidence of the Mohr-Coulomb failure surface with Rankine's one (Figure 3).

2.2 Failure types

In the present work, under plane stress conditions, two types of failure are considered depending on the stress-state at the location of the crack origin: a) tensile failure and b) shear failure. Tensile failure occurs under a stress state of pure tension, i.e. the criterion is violated in the first quadrant in Figure 3, and is characterized by a crack forming in a

direction perpendicular to the maximum principal stress/strain. Shear failure occurs when $\sigma_1\sigma_3 < 0$, viz. the criterion in Figure 3 is violated either in the second or fourth quadrant. Under such conditions, the normal and shear stresses reach a critical combination on two planes. These planes, noted by the points B and B' in Figure 2, are symmetrical with respect to the direction of the minimum principal stress diverging from it by an angle $\beta = \pm\left(\frac{\pi}{4} - \frac{\varphi}{2}\right)$, depending on the frictional characteristics of the material.

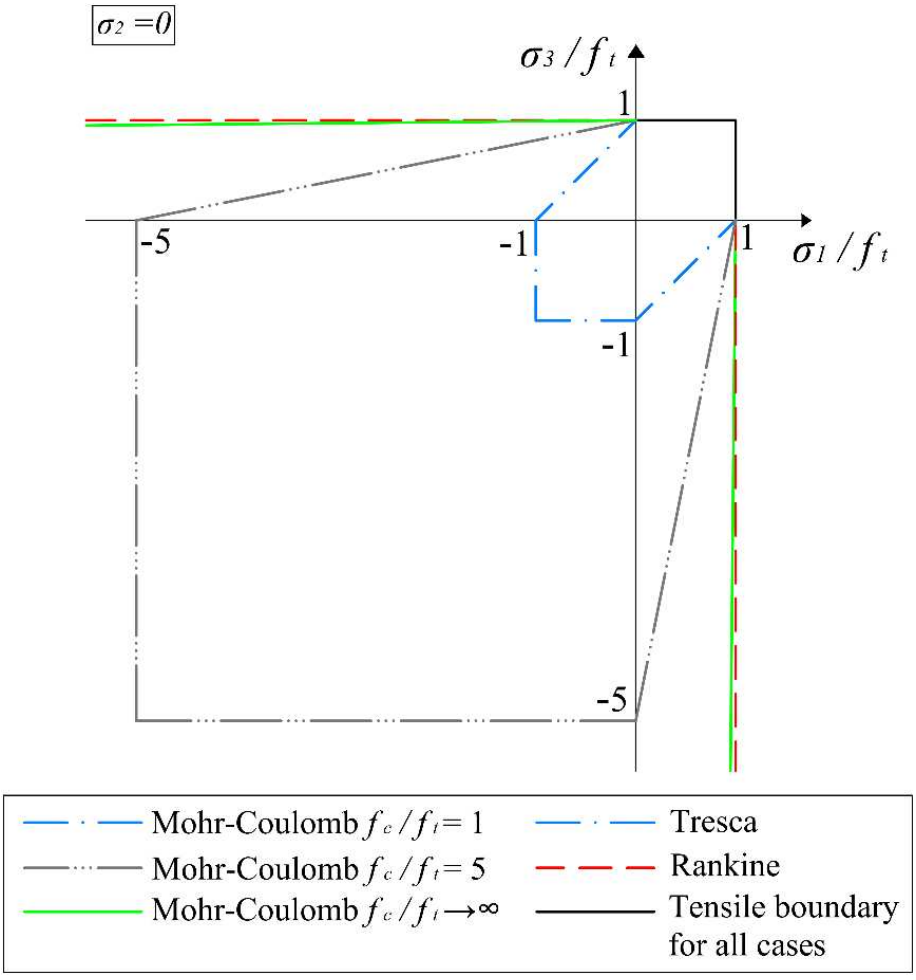

Figure 3. Comparison of Mohr-Coulomb failure criterion with Tresca and Rankine in the biaxial stress plane

3. Continuum damage model

In this work, fracture of material is simulated by the use of a constitutive model based on continuum damage mechanics [Cervera 2003]. This model has proven to be adequate for the analysis of structures made of quasi-brittle materials such as concrete [e.g. Cervera & Chiumenti 2006a, Cervera & Chiumenti 2006b] and masonry [e.g. Pelà et al. 2011, Pelà et al. 2013, Pelà et al. 2014a].

The constitutive equation for the damage model is defined as:

$$\boldsymbol{\sigma} = (1 - d)\bar{\boldsymbol{\sigma}} = (1 - d)\boldsymbol{C}\colon\boldsymbol{\varepsilon} \tag{7}$$

where $\bar{\boldsymbol{\sigma}}$ denotes the effective stress tensor [Lemaitre & Chaboche 1978] computed in terms of the total strain tensor $\boldsymbol{\varepsilon}$ and $\boldsymbol{C}$ is the usual fourth order isotropic linear-elastic constitutive tensor. The damage index d represents the damage state of the material, varying from zero when the material is undamaged to one when the material is completely damaged. In this work, the use of a single damage variable is justified by our aim to investigate fracture due to only tensile and shear stress states. In the general case, where damage due to compression may be critical, an equivalent damage model with two separate damage variables for compressive and tensile damage can be used (see Roca et al. 2013, Petromichelakis et al. 2014, Pelà et al. 2014b, Saloustros et al. 2015).

The equivalent stress is a positive scalar depending on the effective stress tensor and the failure criterion assumed. In the current work, according to the Mohr-Coulomb theory, it assumes the following form:

$$\Sigma = \bar{\sigma}_1 - \frac{f_t}{f_c}\bar{\sigma}_3 \tag{8}$$

where $\bar{\sigma}_1$ and $\bar{\sigma}_3$ are the maximum and minimum effective principal stresses, respectively. The damage criterion can be expressed as:

$$\Phi(\Sigma, r) = \Sigma - r \ \leq 0 \tag{9}$$

The internal stress-like variable r represents the current damage threshold. Its value is determined as the maximum between $r_0 = f_t$ and the greatest value ever attained by the equivalent stress Σ during the loading history [Cervera 2003]:

$$r = \max[r_0, \max(\Sigma)] \tag{10}$$

Following the above, the internal damage variable d can be defined in terms of the corresponding current value of the threshold $d = d(r)$, so that it is a monotonically increasing function such that $0 \leq d \leq 1$. In particular, the following exponential function is considered:

$$d(r) = 1 - \frac{r_0}{r} exp\left\{-2H_d\left(\frac{r - r_0}{r_0}\right)\right\} \qquad r_0 \leq r \tag{11}$$

where $H_d \geq 0$ is the discrete softening parameter. For ensuring mesh-size independence the specific dissipated energy D is adjusted for each damaged finite element so that the equation

$$D l_{dis} = G_f \tag{12}$$

holds, where l_{dis} is the discrete crack characteristic width and G_f the tensile fracture energy of the material. For the isotropic damage model with exponential softening the specific dissipated energy is [Cervera & Chiumenti 2006b]:

$$D = \left(1 + \frac{1}{H_d}\right)\frac{(f_t)^2}{2E} \tag{13}$$

Using Equations (12) and (13) the discrete softening parameter is defined as:

$$H_d = \frac{l_{dis}}{l_{mat} - l_{dis}} \tag{14}$$

where the material characteristic length $l_{mat} = 1/H_{mat}$, with $H_{mat} = (f_t)^2/(2EG_f)$, depends only on the material properties. Finally, the discrete crack characteristic width can be taken as the representative size of the element $l_{dis} = l_e = \sqrt{2A_e}$, being A_e the surface of the triangular element.

4. The local crack-tracking algorithm

The proposed crack-tracking technique is based on the algorithm developed by Cervera and co-workers [Cervera et al. 2010a]. This section includes an overview of the algorithm, focusing on the added features for the simulation of cohesive-frictional damage.

The methodology bases on a labelling system and is applied at the beginning of each load increment. According to the stress field of the previous converged load increment, the

algorithm identifies new cracks within the discretized domain. Following this, the propagation of the old and the new cracks is defined according to the stress state of the *crack tip* or the *crack origin* elements, respectively. Then, the elements lying on the crack path are recognized and labelled as *able to damage*. This labelling system remains unchanged during the equilibrium equations of the current load increment, when the stress field is evaluated activating the constitutive law presented in Section 3 only for the labelled as *able to damage* elements. Figure 4 illustrates the main steps of the proposed algorithm that are detailed in the following sections.

4.1 New crack detection

The crack-tracking algorithm starts with the detection of new cracks. For the purposes of this work, new cracks originate at the boundaries of the domain, at elements satisfying Mohr-Coulomb's failure criterion, as defined in Equation (4). In the case of several elements reaching failure at the same increment, an *exclusion radius criterion* is applied [Cervera et al. 2010a]. Under this criterion, the element with the highest value of $f(\sigma_1, \sigma_3)$ within a defined by the user radius r_{excl} is labelled as a *crack root* element.

4.2 Crack propagation

The next step of the algorithm consists in determining the crack propagation direction for new and old cracks. This procedure takes place either at the *crack root* elements for new cracks or at the *crack tip* elements for consolidated cracks. A *crack tip* element is an element located at the propagating front of an old crack.

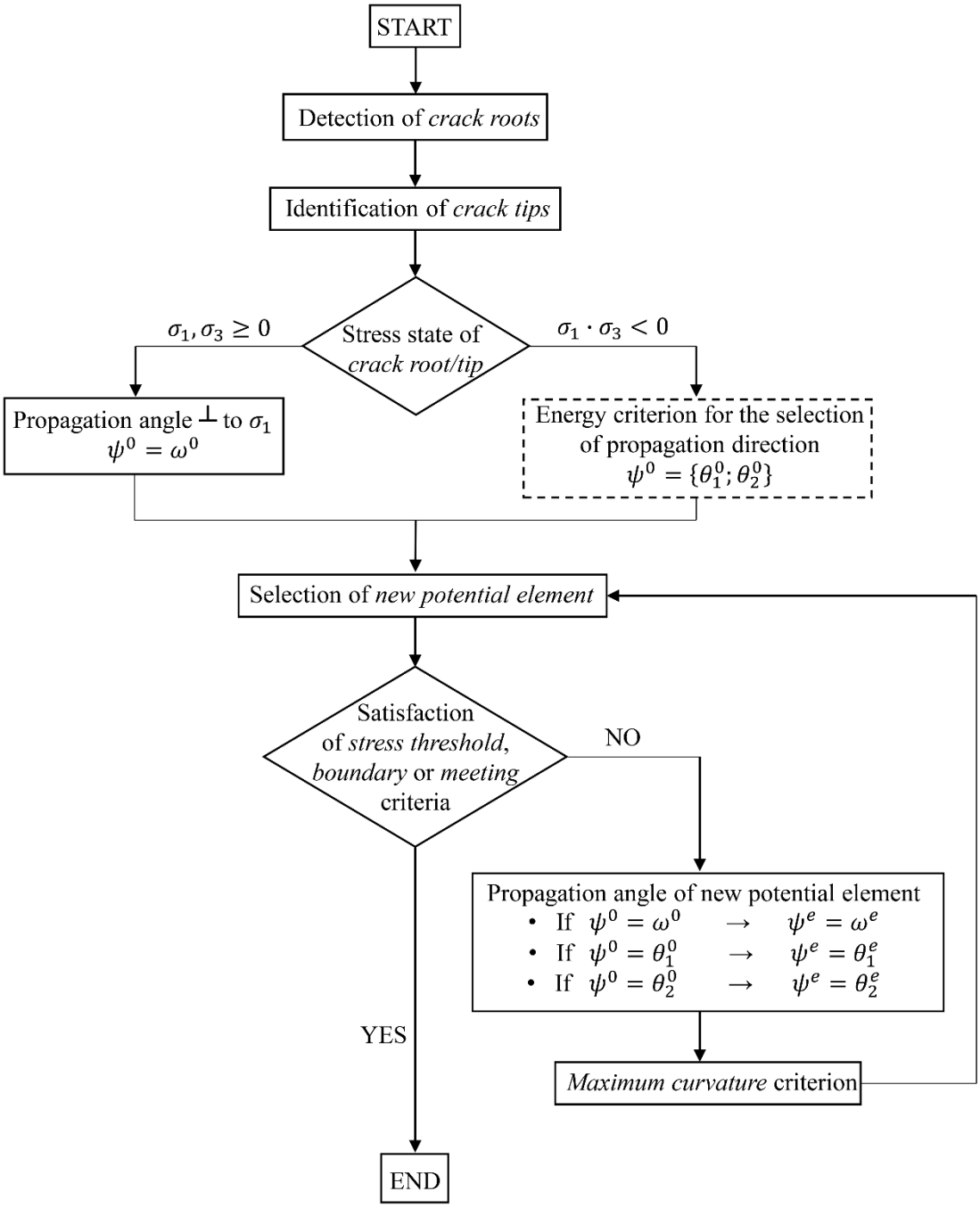

Figure 4. Flowchart with the basic steps of the proposed local crack-tracking algorithm.

Depending on the stress-state of the *crack tip/root* element, two types of failure may occur and, consequently, two alternative values of the propagation angle ψ^0 can be defined for the crack tip element:

a) *Tensile failure.* An element fails in tension when its principal stresses are greater or equal to zero. In this case, the crack propagates towards a direction ω, perpendicular to the direction of the maximum principal stress.

b) *Shear failure.* An element fails in shear when it has at least one tensile and one compressive principal stresses. As described in section 2.2, in this case failure can occur in two possible planes according to the Mohr-Coulomb theory of fracture, see Figure 2. The two possible crack-propagation directions $\theta_{1,2}$ are:

$$\theta_1 = \omega + \left(\frac{\pi}{4} - \frac{\varphi}{2}\right), \qquad \theta_2 = \omega - \left(\frac{\pi}{4} - \frac{\varphi}{2}\right) \qquad \text{(15a-b)}$$

The selection among these two fracture planes is decided in this work with the use of an energy-based criterion that will be presented in Section 4.3.

Once the propagation direction for each crack is decided, then the path of each crack is evaluated and the elements pertaining to it are labelled as *potential elements* to damage in the current load increment. Figure 5b illustrates this procedure. Starting from the *crack tip/root* element, the neighbour element lying on the defined crack propagation direction is labelled as the *new potential element*. To this end two actions are carried-out:

1. Determination of the crack angle of the *new potential element*. During an increment each crack will propagate in the direction determined from the *crack tip/root element*, i.e. either perpendicular to the direction of the maximum principal stress or according

to Equations 15a-b. However, the value of the cracking angle of the *new potential element* (ψ^e) is calculated according to its own stress state and therefore is denoted by $\omega^e, \theta_1^e,$ or θ_2^e.

2. Control and correction of the propagation angle. The *maximum curvature criterion* ensures that no spurious change occurs in the crack direction [Cervera et al. 2010a]. To achieve this purpose, the angle a between the vector $\vec{V}_e$ and the vector $\vec{V}_c$ is calculated. The vector $\vec{V}_e$ denotes the crack direction for the new potential element. The vector $\vec{V}_c$ represents the vector sum of the crack directions of both the potential elements and the consolidated damaged elements within a neighbourhood of radius r_{neigh} (see Figure 5b). The radius r_{neigh} is a length defined by the user and it is measured from the centroid of the *current tip potential* element. In case of $a \leq a_{max}$, the vector $\vec{V}_e$ is used for the crack propagation direction of the new potential element. In case of $a > a_{max}$, the vector $\vec{V}_c$ is used for the definition of the crack propagation direction.

Following these two actions, the *next potential element* lying on the crack path can be recognised. The above procedure continues until two cracks coalesce (*crack meeting criterion*), a crack reaches the mesh boundary (*boundary criterion*) or the value $f(\sigma_1, \sigma_3)$ (see Equation (4)) of the new potential element is lower than a threshold defined by the user (*stress threshold criterion*). In this work the threshold used is $f(\sigma_1, \sigma_3) = -0.25$ [Cervera et al. 2010a].

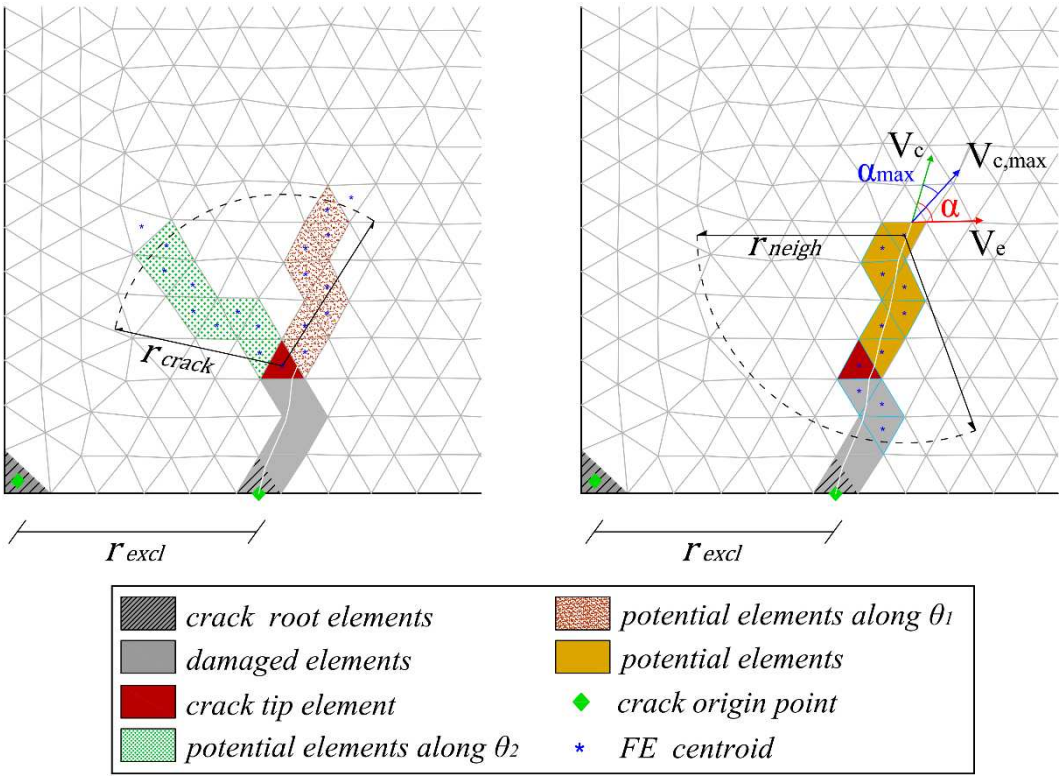

Figure 5. Basic steps of the proposed local crack-tracking algorithm: selection between the two possible crack propagation directions for frictional failure (a) and labelling of potential elements with angle correction (b).

After performing the above procedure for all the new and old cracks of the analysed domain, each element is clarified into two categories. The first one declares the cracking state of the element:

- *Intact & unable to damage element*: element that does not belong to any crack and will remain linear elastic.
- *Intact & able to damage element*: element that belongs to a crack path and it is allowed to damage during the current load increment.

- *Damaged element*: element belonging to a consolidated crack and has entered the non-linear regimen.

The second category denotes the selected crack propagation direction of each damaged element.

- ω: damaged element with crack propagation direction perpendicular to the direction of the maximum principal stress.
- θ_1: damaged element with crack propagation direction equal to $\theta_1 = \omega + (\pi/4 - \varphi/2)$.
- θ_2: damaged element with crack propagation direction equal to $\theta_2 = \omega - (\pi/4 - \varphi/2)$.

4.3 Mohr-Coulomb failure plane selection

The selection between the two possible failure planes proposed by the Mohr-Coulomb theory is of great importance within the proposed algorithm, since it determines the outcome of the crack propagation. In this work, a solution to this dilemma is given by evaluating the elastic strain energy fields of the two possible crack paths prior to their opening. The selected path is the one with the highest stored elastic strain energy. This choice is based on the premise that upon fracture the material neighbouring to the fracture zone will unload elastically. In this way the strain energy release is maximized, minimizing the total strain energy of the body. This procedure also minimizes the energy dissipated during the development of the fracture. Similar criteria have proved to be successful in geotechnical engineering simulations for determining the propagation of fracture in faults (see Olson & Cooke 2005, Okubo & Schultz 2005).

The process for the selection of the crack propagation direction starts after the *crack tip* and *crack root* elements are defined (see Figure 4). Then for each *crack tip/root* element the procedure, illustrated in Figure 6, for determining the crack propagation direction is as follows:

1. The two possible angles for the crack propagation of the *crack tip/root* element are defined.
2. For each of these two angles, the two possible crack paths are determined and the composing potential elements on each of them are defined (Figure 5a). This occurs in the following order:
   i. The crack propagation direction of the *crack tip* element is defined at the direction of θ_1.
   ii. For this crack propagation direction, the *new potential element* is identified.
   iii. The distance δ_κ between the centroid of the *new potential element* and the centroid of the *crack tip/root* element is computed.
   iv. If the *new potential element* lies within the limit of the radius r_{crack} (defined in the step *(vii)* of this section) the total strain energy W^e on the volume V^e are computed:

$$W^e = \int_{V^e} \frac{1}{2} \boldsymbol{\sigma} : \boldsymbol{\varepsilon} \, dV \tag{16}$$

   where $\boldsymbol{\sigma}$ and $\boldsymbol{\varepsilon}$ are the stress and strain tensors of the *new potential element* and V^e is the volume of the element.
   v. The propagation angle of the *new potential element* is calculated and the maximum curvature criterion is applied.

vi. The *new potential element* is named as *current crack tip* and the above steps are repeated.

vii. The procedure stops when the *crack meeting criterion*, *the boundary criterion* or *the crack limit criterion* is satisfied. The first two are the same criteria as described in Section 4.2. The *crack limit criterion* is satisfied when the distance between the *crack tip/root* and the *new potential element* δ_κ overpasses a radius r_{crack} (see Figure 5a). This radius is calculated for each crack at each load increment. It is the minimum between a radius defined by the user r_{crit} and the distance between the *crack tip/root* and the last *potential element* before the crack meets a mesh boundary or another crack.

viii. When one of the above criteria is met, the steps from (ii) to (vii) are repeated with the crack propagation direction of the *crack tip/root* element set as θ_2.

3. To this end, with the composing elements of the two possible cracks and their strain energy and volume defined, the total strain energy per crack volume for each of the two cracks can be defined as:

$$w_1 = \frac{1}{V_1}\sum_i^n W_i^e \qquad\qquad w_2 = \frac{1}{V_2}\sum_j^m W_j^e \qquad (17a\text{-}b)$$

The crack volume at each direction (V_1, V_2) is defined as the sum of the volume of the elements (V^e) pertaining to the crack path,

$$V_1 = \sum_i^n V_i^e, \qquad\qquad V_2 = \sum_j^m V_j^e \qquad (18a\text{-}b)$$

where $i = 1, n$ are the elements on the direction of the crack determined with θ_1 and $j = 1, m$ are the elements on the direction of the crack determined with θ_2.

Finally, the selected crack direction for the particular increment is the direction with the greatest strain energy per crack volume.

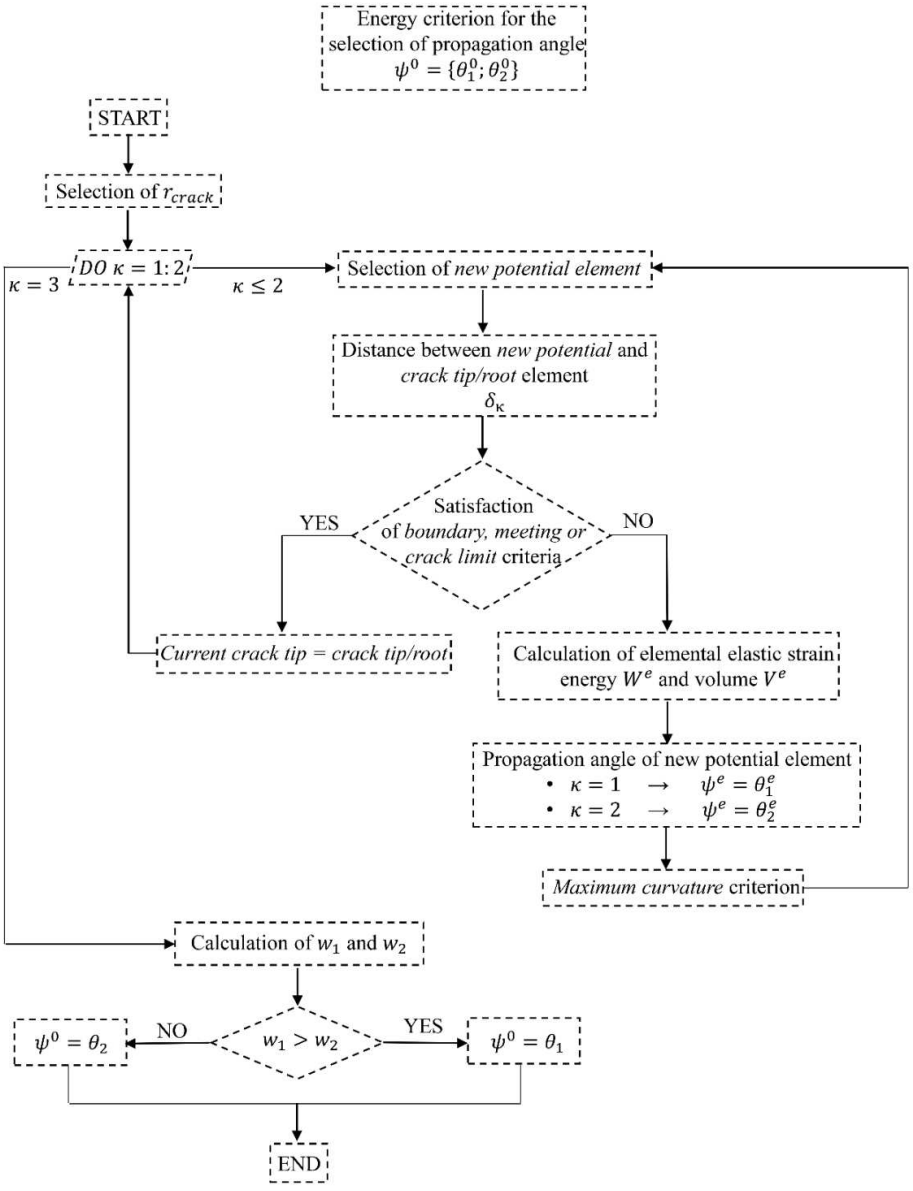

Figure 6. Flowchart with the procedure for the selection of the frictional crack propagation direction θ_1 or θ_2.

5. Numerical Examples

In this section, the proposed formulation is applied to the analysis of three benchmark problems for mixed mode fracture in concrete. They correspond to a series of experiments on a double edge notched (DEN) specimen under non-proportional loading, performed by Nooru-Mohamed [Nooru-Mohamed 1992]. The tested concrete specimen is square shaped with dimensions 200×200×50 mm^3 and two notches with a depth of 25 mm and height of 5 mm at each lateral side. The DEN specimen was glued to four platens in the configuration of Figure 7. The numerical simulations correspond to the load-path 4 of the experimental campaign, which was performed in two steps. In the first one, a compressive load was applied to the lateral platens in displacement control up to a value P_s. Subsequently, a traction load P was applied over the top platen in displacement control keeping the lateral force P_s constant under load control. Figure 8 illustrates the cracking patterns observed at the DEN specimens after the experiments for the load paths 4a (specimen 48-03), 4b (specimen 46-05) and 4c (specimen 47-06) corresponding to lateral force $P_s = 5$ kN, 10 kN and 27.5 kN respectively. Two concrete specimens were tested for load-path 4b, whereas only one specimen was tested for load-paths 4a and 4c,. Nooru-Mohamed mentions that although the experiment itself as well as the experimental apparatus were sophisticatedly designed, undesirable eccentricities in the experiment can be provoked by the skew-symmetric bonding of the specimen to the steel platens, the possible relative rotations between the two used coupled frames and the non-symmetric behaviour of the springs (in the longitudinal direction) that were used to avoid the in-plane rotation of the

DEN specimen. For a comprehensive discussion on the experimental procedure, apparatus and problems the reader is referred to the original work [Nooru-Mohamed 1992 & Nooru-Mohamed et al. 1993].

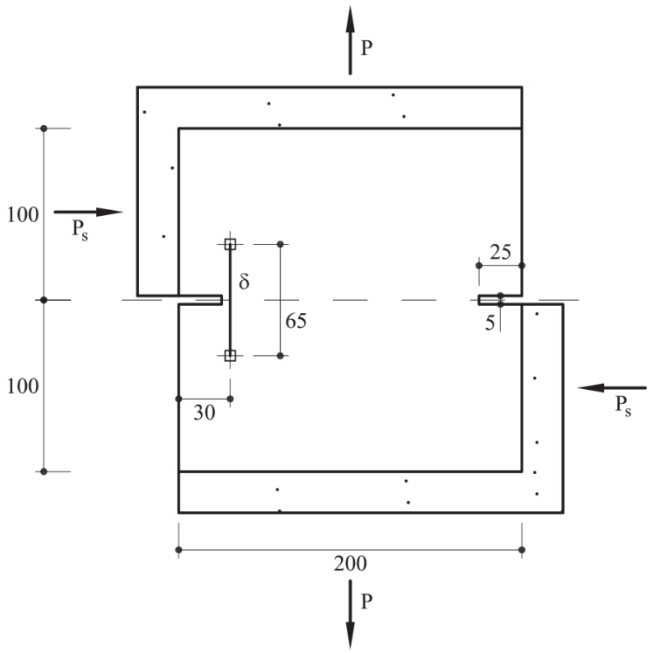

Figure 7. Geometry and load for double edge notched specimen [Nooru-Mohamed 1992]

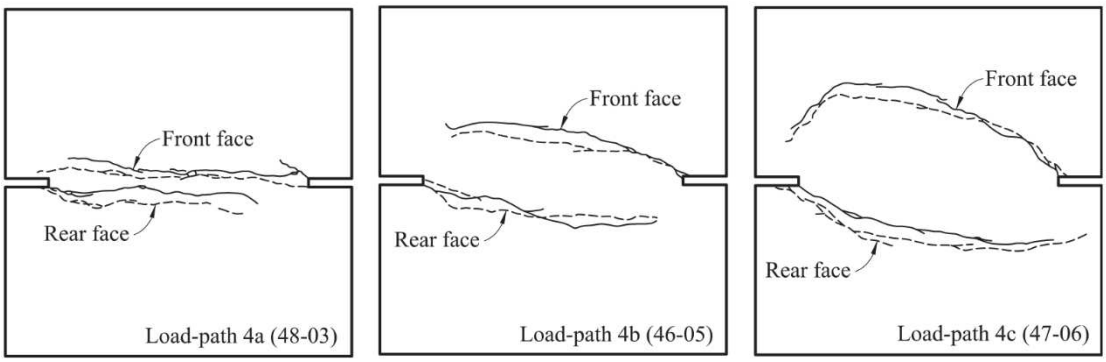

Figure 8. Experimentally obtained crack patterns in the front (solid lines) and rear (dashed lines) faces for double edge notched specimens [Nooru-Mohamed 1992].

The material parameters used for the numerical simulation are based on the data provided by Nooru-Mohamed [Nooru-Mohamed 1992] and are the same for the three different load paths: tensile strength f_t = 3.0 MPa, Young Modulus E = 30 MPa, Poisson's ratio v = 0.2, and mode I fracture energy G_f = 110 J/m^2.

The three experiments are discretized in an unstructured mesh with average mesh size of h_e = 2.5 mm (8394 nodes). For load path 4c a second mesh is used, with average mesh size of h_e = 5 mm (2162 nodes), aiming to investigate the mesh-size and mesh-bias dependency of the algorithm. The discretization consists of 2D plane-stress 3-noded linear triangular elements. The computational boundary conditions are exactly skew-symmetrical, with the central node of the mesh being fixed in the horizontal and vertical degrees of freedom. Regarding the input parameters for the local crack-tracking algorithm, $r_{excl} = 0.12\ m$ and $r_{crit} = 0.03\ m$ for all the presented examples. The definition of a_{max} and r_{neigh} has been unnecessary since no important bending occurs.

Calculations are performed with an enhanced version of the finite element program COMET [Cervera et al. 2002, COMET 2013], while pre and post-processing with GiD [GiD 2014]. Both software have been developed at the International Center for Numerical Methods in Engineering (CIMNE), in Barcelona. The discrete weak form of the problem is solved incrementally in a step-by-step manner. At each load increment, the corresponding nonlinear equations are solved with the use of a modified Newton-Raphson method (using the secant stiffness matrix) along with a line search procedure. Convergence of an

increment is attained when the ratio between the iterative residual forces and the norm of the total residual forces is lower than 0.01 (1%).

The outline of each simulated experiment is as follows. Firstly, the two possible solutions indicated by the Mohr-Coulomb fracture criterion are presented. It is noted that for these analyses the procedure for the angle selection has been turned-off and the angle of the fracture is selected explicitly to be equal to θ_1 or θ_2 according to the studied case. Following this, the capacity of the local crack-tracking algorithm, proposed in Section 4, to model the frictional characteristics of quasi-brittle materials is demonstrated by presenting the numerical solutions for three different compressive to tensile strength ratios $f_c/f_t = 5;\ 20,\ \infty$. For comparison purposes, each example is simulated also with the use of the previous version of the local crack-tracking algorithm based in the Rankine failure criterion [Cervera et al. 2010a].

5.1 Load-path 4a

For load-path 4a the lateral compressive load applied during the first stage of the experiment is $P_s = 5$ kN. At the second stage, the vertical displacement δ is gradually increased keeping the lateral load P_s constant.

As commented, the numerical analysis of the specimen starts by presenting the two possible solutions according to the Mohr-Coulomb postulate, for $f_c/f_t = 20$. Hence, the results presented in Figure 9 have been produced by turning off the procedure described in Section 4.3 for the selection of the crack propagation direction. In these analyses, the fracture under shear propagates at a constant angle θ_1 (Figure 9a) or θ_2 (Figure 9b) de-

pending on the case. Note that when damage occurs under pure tension the fracture propagates at a direction perpendicular to the maximum principal stresses (i.e. ω). It can be seen in Figures 9a and 9b that, for this load-path, the cracking of the specimen is mostly defined by tensile failure. It is only a small part at the middle of the crack that fails under shear and where the direction of the crack is different in the two analysed cases. As a result, the dissipated energy is very similar for both cases. Nevertheless, the less curved crack for a propagation direction θ_1 results in the slightly lower dissipated energy, see Figure 9c.

The capacity of the local crack-tracking algorithm to capture the effect of the material's frictional properties is demonstrated by considering three different compressive to tensile strength ratios: $f_c/f_t = 5;\ 20; \infty$. As shown in Figure 10, the effect of the frictional angle is evident in the crack propagation direction of the part of the crack failing under shear. In the same figure, we can see that the curvature of the crack using the Mohr-Coulomb failure criterion with $f_c/f_t \approx \infty$ (Figure 10c) is identical to that obtained by using Rankine (Figure 10d). This outcome illustrates that the (nonrealistic) use of a friction angle of almost $\pi/2$ results in the coincidence of the Mohr-Coulomb failure criterion with that of the Rankine for tensile and shear stress states ($\varphi \approx \pi/2 \Rightarrow \left(\frac{\pi}{4} - \frac{\varphi}{2}\right) \approx 0$) as presented previously in section 2.1, Figure 3.

The small part of the crack failing under shear leads to the insignificant differences in the dissipated energy for the specific load path for the different values of f_c/f_t, as illustrated in the graph of Figure 10e. In overall, the obtained load vs. displacement curves follow the same pattern as the experimental one presenting a slowly curving part when the cracks

propagate and finally entering into a softening branch upon the cracks have sufficient length to develop the failure mechanism. However, differences exist in terms of peak load and dissipated energy. This divergence has been observed by several authors [e.g., Di Prisco et al. 2000, Unger et al. 2007, DeJong et al. 2008, Roth et al. 2015] simulating the same test and can be possibly attributed to the experimental problems previously described.

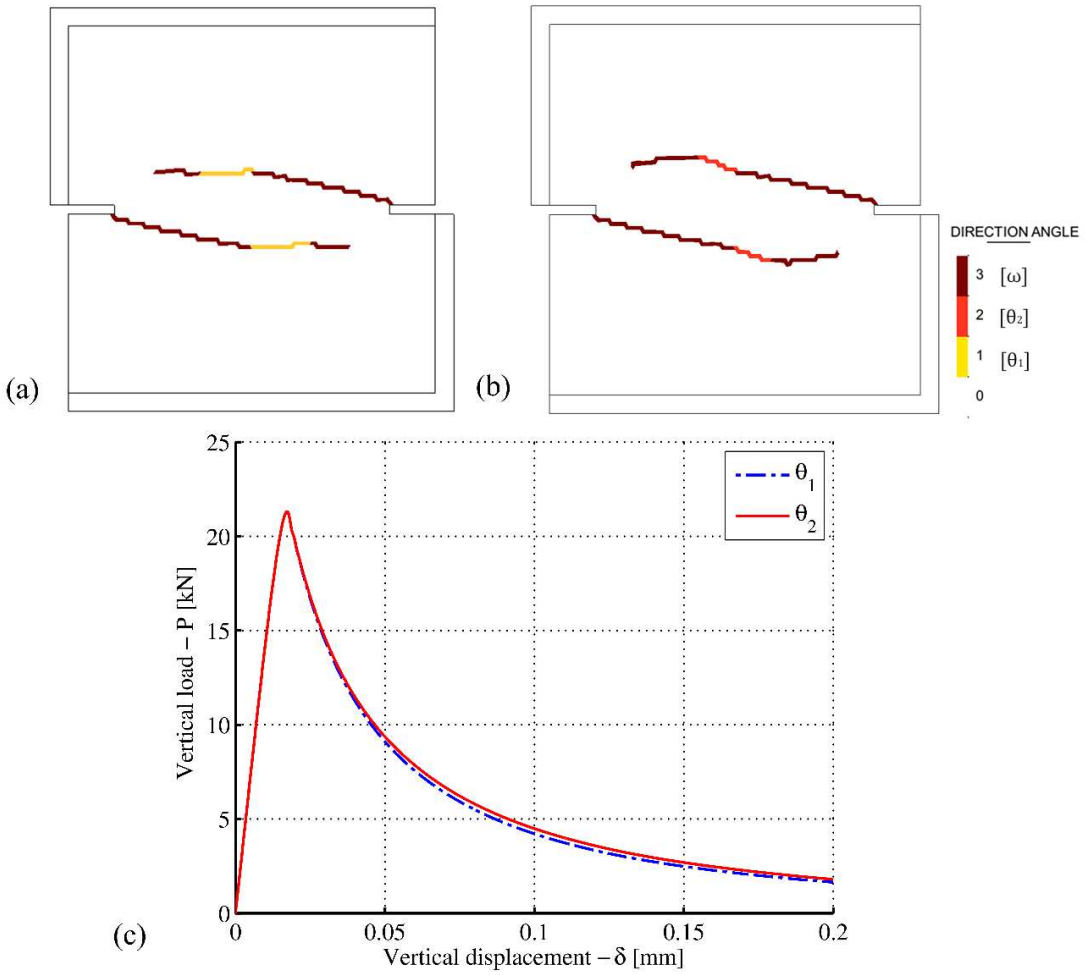

Figure 9. Load-path 4a for $f_c/f_t = 20$: contour of the selected crack propagation direction in the damaged elements case θ_1 (a), case θ_2 (b) and load vs displacement (P-δ) for the two possible fracture planes (c).

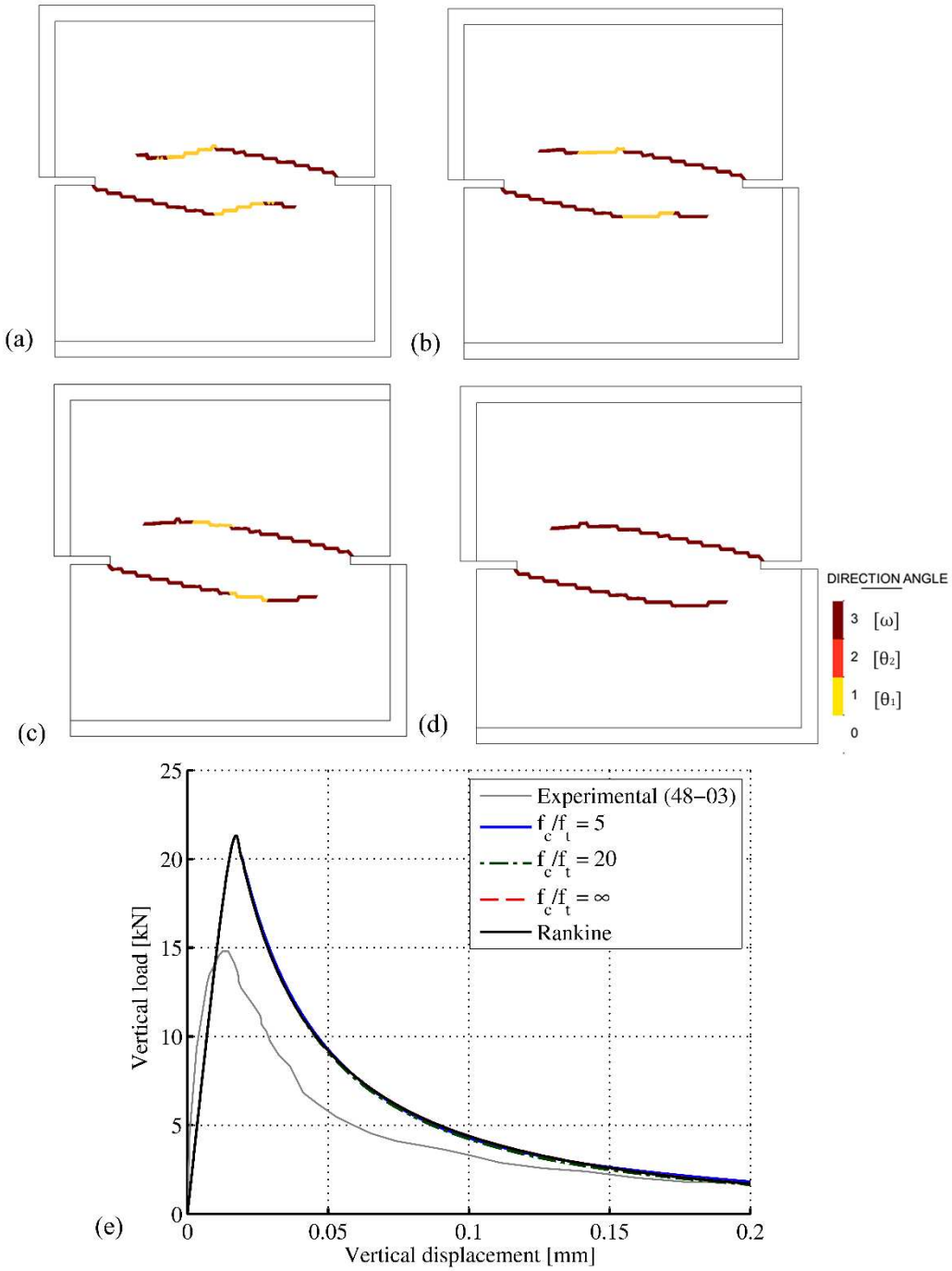

Figure 10. Load-path 4a: contour of the selected crack propagation direction in the damaged elements for Mohr-Coulomb's criterion and $f_c/f_t = 5$ (a), $f_c/f_t = 20$ (b), $f_c/f_t = \infty$ (c); for Rankine's criterion and $f_c/f_t = 20$ (d) and load vs displacement (P-δ) for different compressive to tensile strength ratios (e).

5.2 Load-path 4b

In this load-path the lateral compressive force applied in the first step is $P_s = 10\ kN$. Then, a vertical traction is imposed by increasing gradually the vertical displacement δ under the constant effect of P_s.

As for load-path 4a, first the procedure for the angle selection is turned-off and the two possible solutions according to the Mohr-Coulomb postulate, i.e. θ_1 or θ_2 for failure under shear are presented for $f_c/f_t = 20$. As shown in Figure 11, the two cracks initiate under tension, but soon after, they evolve under a shear stress state. As a consequence, the crack propagation direction plays an important role to both the curvature of the crack and the dissipated energy, which can be appreciated in Figures 11 a & b and Figure 11c, respectively. In this case it is evident that a crack propagating at a direction θ_1 leads to a shorter crack with less curvature and to less dissipated energy.

The effect of the material frictional characteristics is evident in Figure 12, which presents the obtained crack trajectories for $f_c/f_t = 5;\ 20; \infty$. As it is shown, the proposed formulation succeeds both in capturing the frictional properties of the material and in selecting the θ_1 crack propagation direction in all the cases. Smaller compressive to tensile strengths ratios result in a smaller curvature of the crack trajectory and in less dissipated energy (see Figure 12e). For the ratio $f_c/f_t = 5$ the two cracks reach the opposite notch and the specimen starts rotating around the developed compressive strut, resulting in the sudden drop of load, as can be appreciated in Figure 12e. Once again, when a high compressive to tensile strength ratio is selected, the solution approaches the Rankine's one

(see Figure 12c & d). Note that when f_c/f_t tends to infinity the two potential crack propagation directions are almost equal (i.e. $\theta_1 \approx \theta_2$) in Mohr-Coulomb's criterion, resulting in an identical possible crack path in most cases.

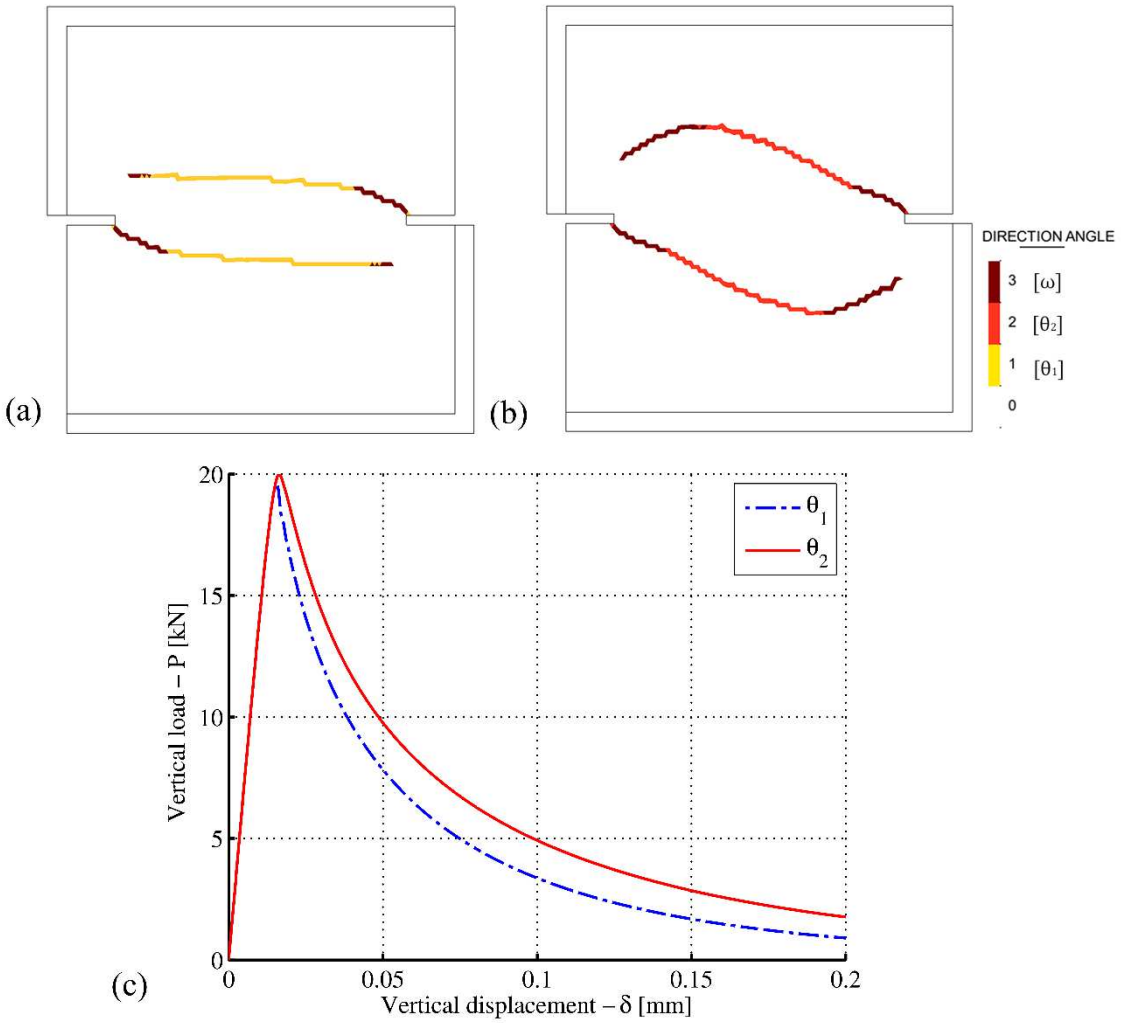

Figure 11. Load-path 4b for $f_c/f_t = 20$: contour of the selected crack propagation direction in the damaged elements: case θ_1 (a), case θ_2 (b) and load vs displacement (P-δ) for the two possible fracture planes (c).

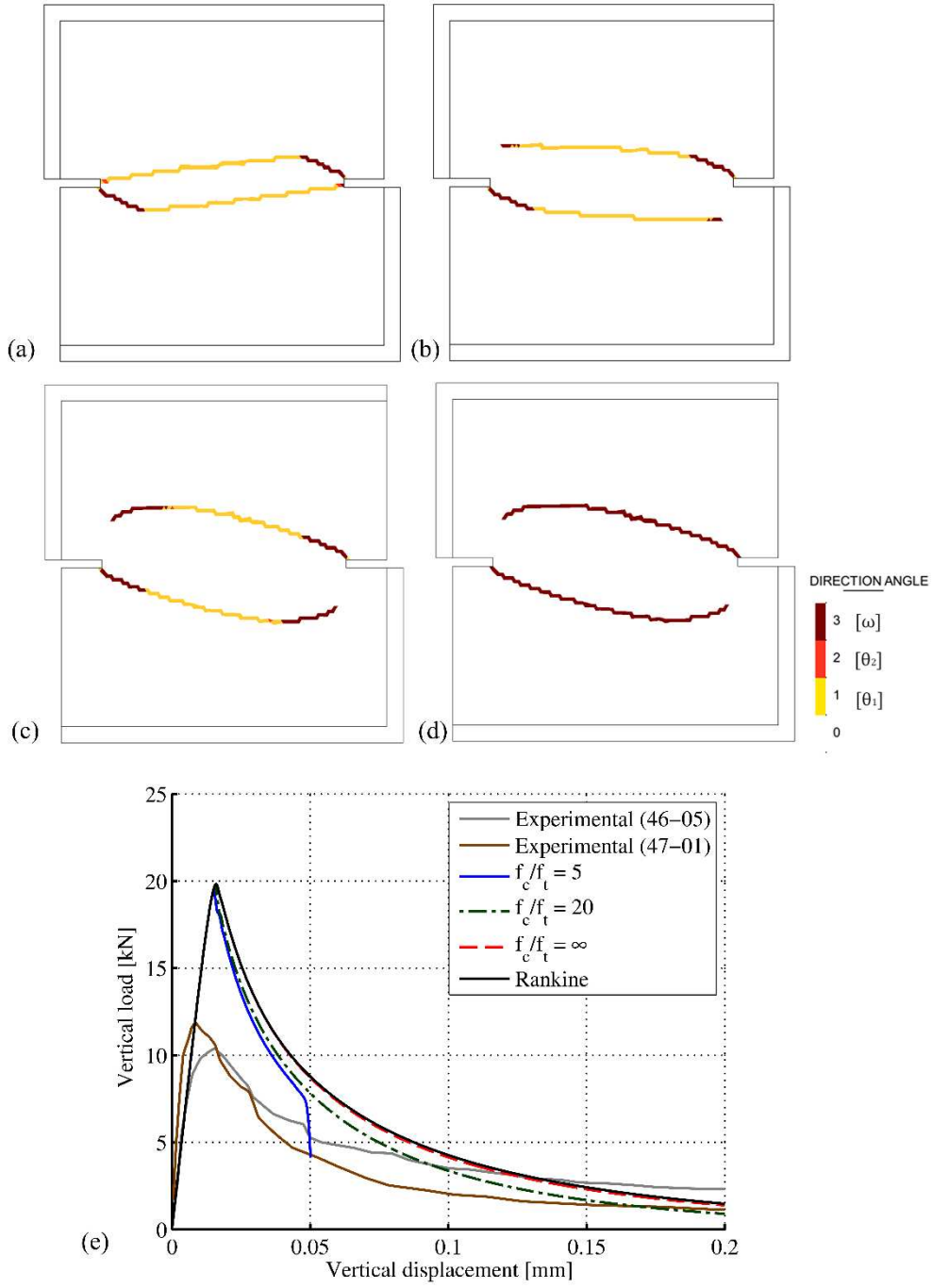

Figure 12. Load-path 4b: contour of the selected crack propagation direction in the damaged elements for Mohr-Coulomb's criterion and $f_c/f_t = 5$ (a), $f_c/f_t = 20$ (b), $f_c/f_t = \infty$ (c); for Rankine's criterion and $f_c/f_t = 20$ (d) and load vs displacement (P-δ) for different compressive to tensile strength ratios (e).

Comparing to the experimental results, the obtained load vs. displacement graphs (Figure 12e) show an overestimation of the predicted peak load. The same discrepancies have been observed in references [e.g. Dumstorff & Meschke 2007, DeJong et al. 2008, Slobbe et al. 2014, Roth et al. 2015]. As commented before, the reason for this divergence may be due to the possible experimental eccentricities.

5.3 Load-path 4c

For load-path 4c the lateral load applied in the first stage P_s is equal to 27.5 kN. During the second stage of the simulation the axial vertical displacement δ is increased under the constant effect of the lateral load P_s.

Figures 13a-b present the two possible crack paths, for $f_c/f_t = 20$, according to the Mohr-Coulomb postulate. Contrarily to the previous two load-paths, and due to the high value of the lateral load P_s, the two cracks start and progress in this case mostly due to shear. Failure under pure tension is visible only at the end of the cracks and when the collapse mechanism is completely developed. As a consequence, the difference between the crack trajectories is important for the two possible crack propagation directions θ_1 and θ_2. This importance of the selected crack path is also reflected in the difference of the dissipated energy visible in the load vs. displacement curves of Figure 13c.

Figure 14 presents the solutions using the proposed algorithm with two different meshes, including the procedure for selecting among the two possible crack propagation directions of Section 4.3. As shown, the crack propagation direction θ_1, which requires less dissipated energy to form, has been correctly selected independently of the degree of refinement of the mesh. The difference in the level of discretization can be appreciated in Figure

14a and Figure 14b. In both cases two skew-symmetric cracks start from the two notches and propagate towards the interior of the specimen. The crack curvature is very similar for the two meshes and no spurious mesh bias is observed. Figure 14c shows the load versus displacement curves for these two simulations. The two graphs present the same trend, with the dissipated energy being almost identical upon mesh-refinement.

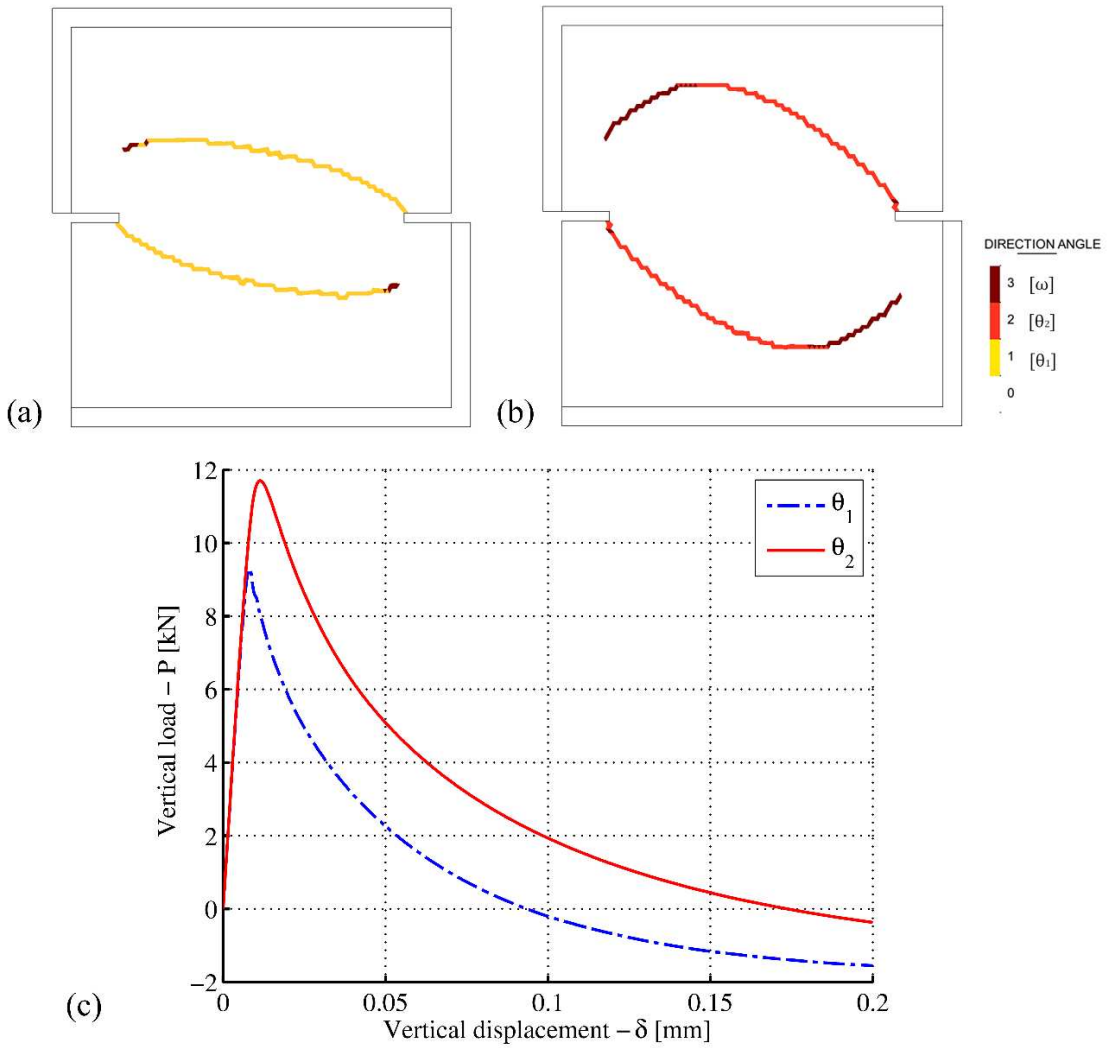

Figure 13. Load-path 4c for $f_c/f_t = 20$: contour of the selected crack propagation direction in the damaged elements: case θ_1 (a), case θ_2 (b) and load vs displacement (P-δ) for the two possible fracture planes (c).

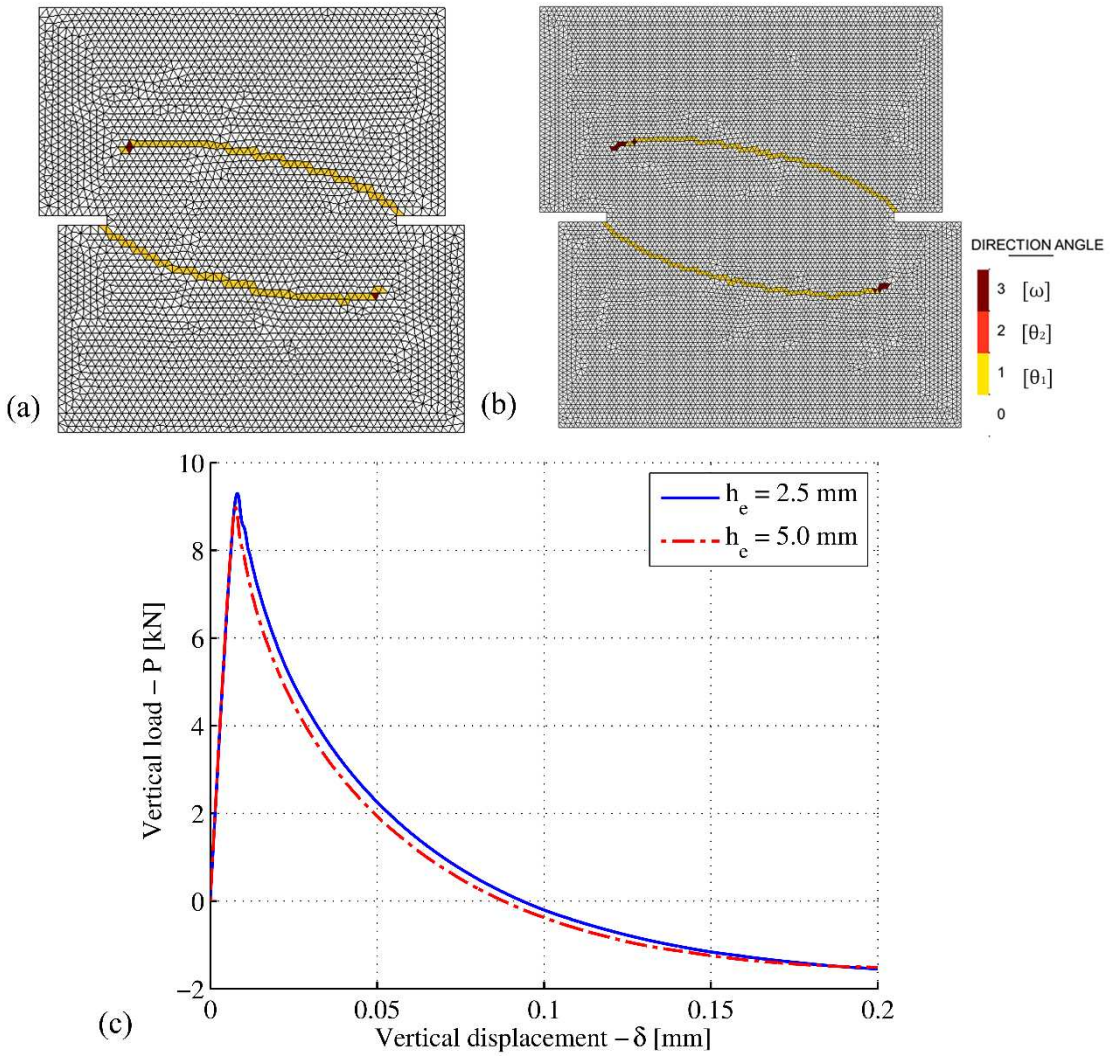

Figure 14. Load-path 4c: contour of the selected crack propagation direction in the damaged elements for mesh with element size h_e = 5.0 mm (a) and h_e = 2.5 mm (b) and load vs. displacement (P-δ) for two different meshes (c).

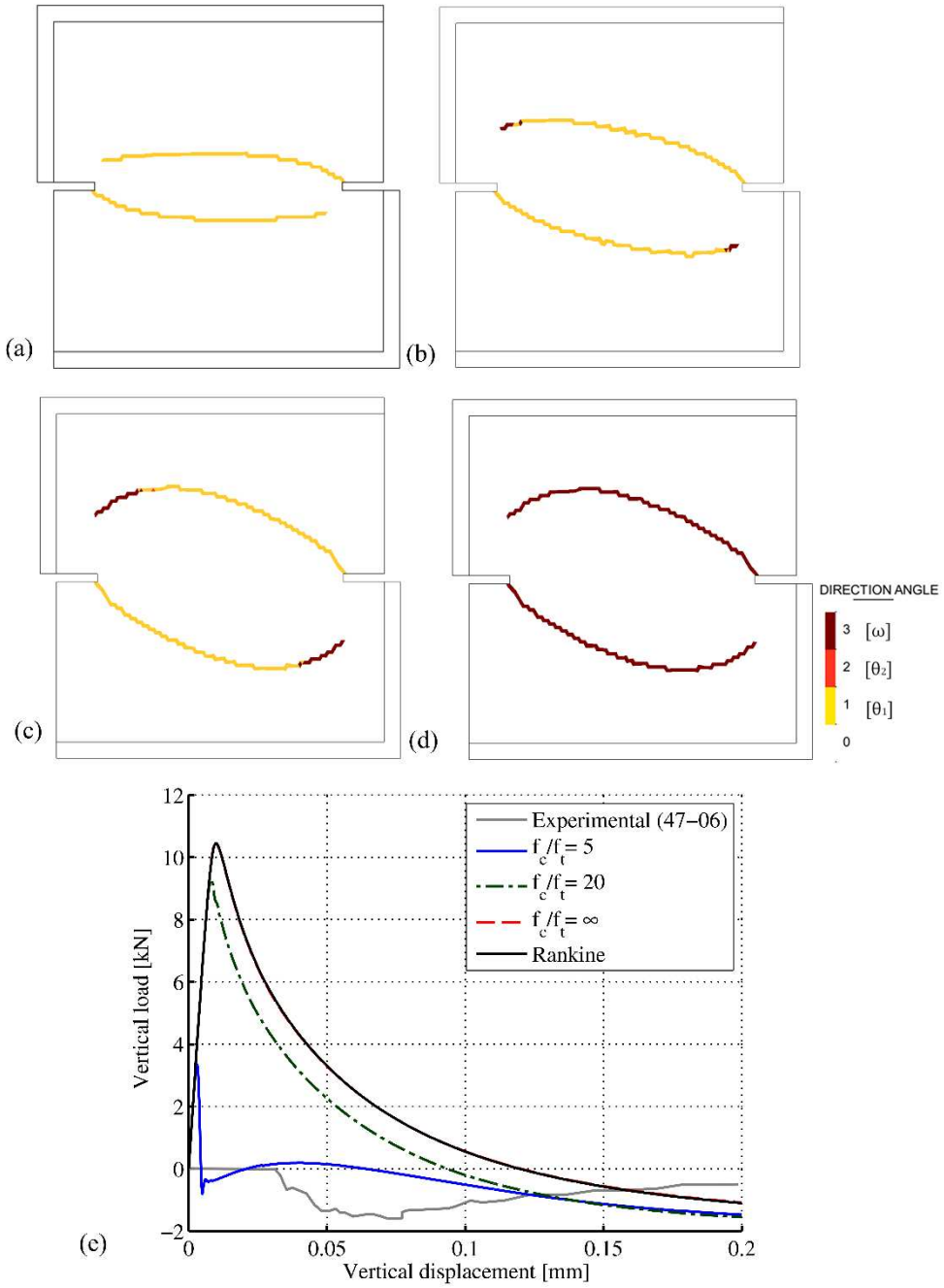

Figure 15. Load-path 4c: contour of the selected crack propagation direction in the damaged elements for Mohr-Coulomb's criterion and $f_c/f_t = 5$ (a), $f_c/f_t = 20$ (b), $f_c/f_t = \infty$ (c); for Rankine's criterion and $f_c/f_t = 20$ (d) and load vs displacement (P-δ) for different compressive to tensile strength ratios (e).

Figure 15 shows the effect of f_c/f_t for load-path 4c in the obtained crack trajectories. Due to the shear failure that occurs along the greatest length of the crack, the effect of the f_c/f_t is clearly observed also in the load vs. displacement curves, presented in Figure 15e. As for load-path 4b, for a ratio $f_c/f_t = 5$ the two cracks form for very small values of vertical load, resulting in the sudden drop of the load and the rotation of the upper and lower parts of the specimen afterwards. Once again, the coincidence between the Mohr-Coulomb criterion with $f_c/f_t \approx \infty$ and the Rankine solution is evident both in terms of the crack-trajectory (Figure 15c & d) as well as of the dissipated energy (Figure 15e). Note that the proposed algorithm succeeds in selecting the crack propagation direction that minimizes the dissipated energy for all the studied ratios of f_c/f_t.

In general, the load displacement graphs attain the same shape as in the previous cases. However, the applied load needs to become compressive to keep stable the propagation of the crack. In the experimental results, a vertical compressive load needs to be applied from the beginning of the second stage of the experiment. This is related to the opening of the bottom crack during the application of the lateral force P_s at the first stage of the experiment, as reported by the authors of the experiments [Noouru-Mohamed 1992]. The fact that the rear side of the same crack opened later comparing to the front side reveals the out-of-plane bending effects experienced by the specimen, which may have affected the experiment and have led to the observed differences between numerical and experimental outcomes [e.g. Dumstorff & Meschke 2007, Roth et al. 2015]. As a result of the earlier cracking at the left notch, the experimental obtained crack trajectory of the lower and upper crack is different. Contrarily, in the numerical solution the two cracks show an almost perfect skew-symmetry.

6. Conclusions

This paper has presented a crack-tracking algorithm oriented to the study of fracture in quasi-brittle materials with cohesive-frictional behaviour. To this aim, a new crack-propagation criterion is proposed that is consistent with the failure types suggested by the Mohr-Coulomb theory failure criterion under shear failure. This methodology extends the applicability of crack-tracking algorithms combined with the smeared crack approach to the simulation of mixed mode loading conditions in a larger family of construction materials.

The proposed crack-tracking algorithm categorizes cracking into shear and tensile. Under pure tension, cracking propagates towards a direction perpendicular to the direction of the maximum principal stress, whereas under shear cracking occurs at a failure plane proposed by the Mohr-Coulomb theory. As shown from the simulated experiments, this separation of the crack regimens is a valuable tool for understanding fracture phenomena in mixed mode problems. Another special feature of the presented algorithm is the ability to select among the two mutually possible fracture planes proposed by the Mohr-Coulomb failure criterion. To achieve this, an energy based criterion is applied at the propagating front of each crack prior to the crack opening. This procedure has proved capable to identify the crack path that maximizes the released strain energy and minimizes the dissipated energy in cracking of concrete under non-proportional loading.

The presented crack-tracking algorithm results in mesh-bias independency of the numerical solution, while the use of the local continuum damage model ensures mesh-size independency. These features allow for the realistic, in qualitative and quantitative terms,

numerical simulation of cracking phenomena in geomaterials within the framework of the smeared crack approach. Additionally, the proposed algorithm offers a numerical solution with reasonable computational cost, since the overhead of using the crack-tracking technique is relatively small. This makes the study of structures with multiple cracks feasible. The proposed algorithm can be easily combined with different constitutive models or with discrete approaches such as the X-FEM and E-FEM.

7. Acknowledgments

This research has received the financial support from the MINECO (Ministerio de Economia y Competitividad of the Spanish Government) and the ERDF (European Regional Development Fund) through the MICROPAR project (Identification of mechanical and strength parameters of structural masonry by experimental methods and numerical micro-modelling, ref num. BIA2012-32234) and from the Excellence Programme for Knowledge Generation by MINECO, through the EACY project (Enhanced accuracy computational and experimental framework for strain localization and failure mechanisms, ref. MAT2013-48624-C2-1-P).

8. References

Benedetti, L., Cervera, M. & Chiumenti, M., 2015. Stress-accurate Mixed FEM for soil failure under shallow foundations involving strain localization in plasticity. *Computers and Geotechnics*, 64, pp.32–47.

Cendón, D.A., Gálvez, J.C., Elices, M., Planas, J., 2000. Modelling the fracture of concrete under mixed loading. *International Journal of Fracture*, 103(3), pp.293–310.

Cervera, M., Agelet de Saracibar, C., Chiumenti, M., 2002. COMET: COupled MEchanical and Thermal analysis, Data Input Manual, Version 5.0, *Technical Report IT-308*. Available from: http://www.cimne.upc.es .

Cervera M., 2003. Viscoelasticity and rate-dependent continuum damage models. CIMNE, *Monography N-79*, Barcelona (Spain): Technical University of Catalunya.

Cervera, M. & Chiumenti, M., 2006a. Smeared crack approach: back to the original track. *International Journal for Numerical and Analytical Methods in Geomechanics*, 30(12), pp.1173–1199.

Cervera, M. & Chiumenti, M., 2006b. Mesh objective tensile cracking via a local continuum damage model and a crack-tracking technique. *Computer Methods in Applied Mechanics and Engineering*, 196(1-3), pp.304–320.

Cervera, M., Pelá, L., Clemente, R., Roca, P., 2010a. A crack-tracking technique for localized damage in quasi-brittle materials. *Engineering Fracture Mechanics*, 77(13), pp.2431–2450.

Cervera, M., Chiumenti, M. & Codina, R., 2010b. Mixed stabilized finite element methods in nonlinear solid mechanics. Part I: Formulation. *Computer Methods in Applied Mechanics and Engineering,* 199, pp.2559–2570.

Cervera, M., Chiumenti, M., Codina, R. 2010c. Mixed stabilized finite element methods in nonlinear solid mechanics. Part II: Strain localization. *Computer Methods in Applied Mechanics and Engineering*, 199 pp.2571-2589

Cervera, M., Chiumenti, M. & Di Capua, D., 2012. Benchmarking on bifurcation and localization in J2 plasticity for plane stress and plane strain conditions. *Computer Methods in Applied Mechanics and Engineering*, 241-244, pp.206–224.

Cervera, M., Chiumenti, M., Benedetti, L., Codina, R., 2015. Mixed stabilized finite element methods in nonlinear solid mechanics. Part III: Compressible and incompressible plasticity. *Computer Methods in Applied Mechanics and Engineering*, 285, pp.752–775.

COMET: Coupled Mechanical and Thermal analysis (2013). http://www.cimne.com/comet/

De Borst, R., 2001. Fracture in quasi-brittle materials: A review of continuum damage-based approaches. *Engineering Fracture Mechanics*, 69, pp.95–112.

DeJong, M.J., Hendriks, M. a. N. & Rots, J.G., 2008. Sequentially linear analysis of fracture under non-proportional loading. *Engineering Fracture Mechanics*, 75(18), pp.5042–5056.

Di Prisco, M., Ferrara, L., Meftah, F., Pamin, J., De Borst, R., Mazars, J., Reynouard, J.M., 2000. Mixed mode fracture in plain and reinforced concrete: Some results on benchmark tests. *International Journal of Fracture*, 103(1991), pp.127–148.

Dumstorff, P. & Meschke, G., 2007. Crack propagation criteria in the framework of X-FEM-based structural analyses. *International Journal for Numerical and Analytical Methods in Geomechanics*, pp.239–259.

GiD: the personal pre and post-processor. Barcelona: CIMNE; 2014. http://www.gidhome.com/ .

Jirásek, M. & Zimmermann, T., 2001. Embedded crack model. Part II. Combination with smeared cracks. *International Journal for Numerical Methods in Engineering*, 50(6), pp.1291–1305.

Jirásek, M. & Belytschko, T., 2002. Computational resolution of strong discontinuities. *Fifth world congress on computational mechanics*, Vienna, Austria; pp.7–12.

Karihaloo, B.L. & Xiao, Q.Z., 2003. Modelling of stationary and growing cracks in FE framework without remeshing: A state-of-the-art review. *Computers and Structures*, 81, pp.119–129.

Lemaitre J, Chaboche JL., 1978. Aspects phénoménologiques de la rupture par endommagement. *J Méc Appl,* 2, pp.317–365.

Meschke, G. & Dumstorff, P., 2007. Energy-based modelling of cohesive and cohesionless cracks via X-FEM. Computer Methods in Applied Mechanics and Engineering, 196(21-24), pp.2338–2357.

Moës, N. & Belytschko, T., 2002. Extended finite element method for cohesive crack growth. *Engineering Fracture Mechanics*, 69(7), pp.813–833.

Nooru-Mohamed, M., 1992. Mixed-mode fracture of concrete: an experimental approach. PhD, Delft University of Technology.

Nooru-Mohamed, M.B., Schlangen, E. & van Mier, J.G.M., 1993. Experimental and numerical study on the behavior of concrete subjected to biaxial tension and shear. *Advanced Cement Based Materials*, 1(1), pp.22–37.

Okubo, C. & Schultz, R., 2005. Evolution of damage zone geometry and intensity in porous sandstone: insight gained from strain energy density. *Journal of the Geological Society*, 162(Engelder 1974), pp.939–949.

Oliver, J. & Huespe, A.E., 2004. Theoretical and computational issues in modelling material failure in strong discontinuity scenarios. *Computer Methods in Applied Mechanics and Engineering*, 193(27-29), pp.2987–3014.

Oliver, J., Huespe, A.E., Samaniego, E., Chaves, E.W.V., 2004. Continuum approach to the numerical simulation of material failure in concrete. *International Journal for Numerical and Analytical Methods in Geomechanics*, 28(78), pp.609–632.

Olson, E.L. & Cooke, M.L., 2005. Application of three fault growth criteria to the Puente Hills thrust system, Los Angeles, California, USA. *Journal of Structural Geology*, 27(10), pp.1765–1777.

Pelà L, Cervera M, Roca P. Continuum damage model for orthotropic materials: application to masonry. *Computer Methods in Applied Mechanics and Engineering* 2011;200:917–30.

Pelà L, Cervera M, Roca P. 2013. An orthotropic damage model for the analysis of masonry structures. *Construction and Building Materials,* 41, pp. 957–67.

Pelà, L., Cervera, M., Oller, S., Chiumenti, M., 2014a. A localized mapped damage model for orthotropic materials. *Engineering Fracture Mechanics*, 124-125, pp.196–216.

Pelà, L., Bourgeois, J., Roca, P., Cervera, M., Chiumenti, M., 2014b. Analysis of the Effect of Provisional Ties on the Construction and Current Deformation of Mallorca Cathedral. *International Journal of Architectural Heritage*, doi: 10.1080/15583058.2014.996920

Petromichelakis, Y., Saloustros, S. & Pelà, L., 2014. Seismic assessment of historical masonry construction including uncertainty. In Á. Cunha et al*., eds. Proceedings of EuroDyn 2014*, pp. 297–304.

Rabczuk, T., 2012. Computational Methods for Fracture in Brittle and Quasi-Brittle Solids : State-of-the-art Review and Future Perspectives. *ISRN Applied Mathematics*, 2013, pp.1–61.

Roca, P., Cervera, M., Pelá L., Clemente, R., Chiumenti, M., 2013. Continuum FE models for the analysis of Mallorca Cathedral. *Engineering Structures*, 46, pp.653–670.

Roth, S.-N., Léger, P. & Soulaïmani, A., 2015. A combined XFEM–damage mechanics approach for concrete crack propagation. *Computer Methods in Applied Mechanics and Engineering*, 283, pp.923–955.

Saloustros, S., Pelà, L., Roca, P. and Portal, J. 2015. Numerical analysis of structural damage in the church of the Poblet monastery. *Engineering Failure Analysis*, 48, pp. 41-61.

Slobbe, A.T., Hendriks, M. a. N. & Rots, J.G., 2014. Smoothing the propagation of smeared cracks. *Engineering Fracture Mechanics*, 132, pp.147–168.

Stolarska, M., Chopp, D.L., Moës, N., Belytschko, T., 2001. Modelling crack growth by level sets in the extended finite element method. *International Journal for Numerical Methods in Engineering*, 51(8), pp.943–960.

Unger, J.F., Eckardt, S. & Könke, C., 2007. Modelling of cohesive crack growth in concrete structures with the extended finite element method. *Computer Methods in Applied Mechanics and Engineerin*g, 196, pp.4087–4100.

Wells, G.N. & Sluys, L.J., 2001. A new method for modelling cohesive cracks using finite elements. *International Journal for Numerical Methods in Engineering*, 50(12), pp.2667–2682.

Wu, J.-Y., & Cervera, M., 2015. On the equivalence between traction- and stress-based approaches for the modelling of localized failure in solids. Submitted to *Journal of the Mechanics and Physics of Solids*, http://dx.doi.org/10.13140/2.1.2589.1200.

Zi, G. & Belytschko, T., 2003. New crack-tip elements for XFEM and applications to cohesive cracks. *International Journal for Numerical Methods in Engineering*, 57(15), pp.2221–2240.